https://doi.org/10.5194/wes-2026-104
Preprint. Discussion started: 3 July 2026

eawe european academy of wind energy
Open Access WIND ENERGY SCIENCE DISCUSSIONS

Automotive lidars for rotating wind turbine blade monitoring

Liqin Jin and Jakob Mann
Department of Wind and Energy Systems, Technical University of Denmark, Frederiksborgvej 399, 4000 Roskilde, Denmark
Correspondence: Liqin Jin (liqn@dtu.dk)

Abstract. Permanently integrated sensor systems, such as strain gauges and fiber optic sensors, are the predominant means of measuring deflection in full-scale wind turbine blades. However, these approaches suffer from several key limitations, including complex calibration procedures, labor-intensive installation, and the inability to repair sensors once the blade structure is sealed. Furthermore, they are severely limited in measuring torsional deformation, a parameter of increasing importance for large wind turbine blades. To address these limitations, this study presents a novel non-contact monitoring framework based on a synchronized array of three automotive-grade lidars, enabling full-scale measurement of blade deflection and torsional deformation under diverse operating conditions. Lidar-derived flapwise deflection measurements (sampled at 33.3 Hz) are validated against co-located strain gauge data acquired at 1.4 m from the rotor plane center (sampled at 50 Hz), while lidar-based pitch angle estimates are validated against SCADA measurements after both signals are resampled to 2 Hz. The measured blade torsional deformation reaches approximately 0.8° under above-rated wind speed conditions, consistent with expected aerodynamic behavior. The dependence of median flapwise deflection on mean hub-height wind speed, rotor azimuth angle, and wind shear is also systematically analyzed. The results demonstrate that the proposed lidar-based system can accurately capture both flapwise deflection and pitch deformation along the blade span. These findings highlight the potential of cost-effective automotive lidar sensors for reliable, high-resolution monitoring of wind turbine structural dynamics under challenging field conditions.

1 Introduction

From industry experts to world leaders and the public, the call to make the global energy sector more sustainable is strong. Although fossil fuels remain the dominant source of electricity generation worldwide, renewable energy already accounts for approximately 30% of global electricity supply (Bouckaert et al., 2021). Looking ahead, the International Energy Agency's Net Zero Emissions by 2050 scenario projects that renewable energy will provide nearly 90% of global electricity generation by mid-century, with wind and solar photovoltaic technologies jointly supplying almost 70% of total electricity demand (IEA, 2023). These projections highlight the pivotal role of wind energy in the decarbonization of future power systems.

Driven by this growing demand, wind energy has expanded rapidly over the past decade and has become one of the most cost-competitive sources of electricity generation. Its deployment is now widely recognized as essential for reducing CO_2 emissions and limiting climate change impacts (Pietzcker et al., 2017; Bistline et al., 2018; Lazard, 2019). To further improve energy capture and reduce the levelized cost of energy, the wind industry has continuously increased turbine size. This trend

https://doi.org/10.5194/wes-2026-104
Preprint. Discussion started: 3 July 2026

eawe european academy of wind energy
Open Access WIND ENERGY SCIENCE DISCUSSIONS

is particularly evident in the offshore sector, where recent turbine designs exceed 20 MW in rated power and feature rotor diameters approaching 300 m with hub heights greater than 150 m (Zahle et al., 2024).

To deliver their designed power output, wind turbines, the world's largest dynamic rotating machines, must operate reliably and safely across a diverse range of environmental conditions. Continuous structural health monitoring of key components, including the generator, gearbox, bearings, rotor, and blades, is therefore essential for improving overall turbine reliability and represents a significant enhancement for operators. This need is especially critical for blades, which endure substantial time-varying aerodynamic loads that can cause material fatigue or excessive bending, ultimately increasing the risk of a tower strike or blade failure (Qiao and Lu, 2015a, b; Grundkötter and Melbert, 2022), as shown in Figure 1.

(a) (b)

Figure 1. Examples of extreme turbine blade deformation and failure: (a) An onshore wind turbine experiencing extreme bending (photo credit: Xumeng Zheng); (b) Vineyard turbine collapsed in 2019 (photo credit: Kit Noble).

The challenge is further compounded by the ongoing trend toward larger and more slender blades (Lehnhoff et al., 2020), which reduces their relative bending stiffness and increases structural compliance, making them more susceptible to deformation-induced failures and exacerbated fatigue damage over their operational lifetime. Structural integrity assessments of wind turbine blades rely primarily on two key parameters: blade deflection and torsional twist. These are governed by a combination of environmental conditions (e.g., ice, sand, and rain) (Mishnaevsky Jr, 2019), gravitational and aerodynamic loading conditions (including wind speed, turbulence, wind shear, and tower stagnation effect), and structural characteristics such as geometry and material properties).

https://doi.org/10.5194/wes-2026-104
Preprint. Discussion started: 3 July 2026

eawe european academy of wind energy
Open Access WIND ENERGY SCIENCE DISCUSSIONS

Real-time monitoring of blade deformation, which can improve total energy efficiency through a controlled safety margin, is supported by several commercially available technologies. Conventional wind turbine blade monitoring systems typically rely on embedded sensors, such as strain gauges and fiber-optic sensor arrays, to capture dynamic structural responses and support damage detection. In strain-based estimation approaches, an optimal sensor configuration must be determined, and a linear relationship between strain and deflection must be established, commonly represented through a transformation matrix (Lee et al., 2017). Optical fiber sensors have also been widely applied due to their low sensitivity to electromagnetic interference and inherent immunity to lightning strikes. These characteristics make them particularly suitable for damage detection and monitoring structural responses, such as bending loads (Schroeder et al., 2006; Lally et al., 2012; Arsenault et al., 2013).

Despite their demonstrated effectiveness and accuracy, embedded sensor systems face significant practical limitations. For example, instrumentation of a 50-meter utility-scale blade may require approximately 200 strain gauges due to their point-sensing nature (Amador et al., 2024) and entails a three-week installation period (Poozesh et al., 2017). Furthermore, strain gauges demand careful and complex calibration (Kverno et al., 2023) and have limited ability to capture torsional twist. Although optical fiber sensors enable distributed sensing, their deployment remains challenging due to complex and precision-sensitive installation procedures, while signal artifacts often require advanced post-processing for reliable interpretation (Fallais et al., 2024). Additionally, embedded sensing systems are constrained by the high cost of high-accuracy sensors and by the fact that faulty sensors are generally inaccessible for repair once the blade structure is sealed (Mäder et al., 2017).

To address the limitations of embedded sensors, increasing attention has been directed toward non-destructive evaluation (NDE) techniques. These methods are being explored for structural health monitoring of external components, including blades and foundations, as well as for condition monitoring of high-speed rotating machinery components (Civera and Surace, 2022). Among them, digital image correlation has emerged as an established technique for full-scale strain measurement of turbine blades, particularly when integrated with drone-based imaging systems (Carr et al., 2016; Wu et al., 2019; Khadka et al., 2019). Laser-based techniques, such as laser Doppler velocimetry and shearography, have also been investigated for deformation and vibration assessment (Hung, 1999; Marks et al., 2017). More recently, video spectroscopy has been proposed as a promising approach for such measurements, although its application to wind turbines remains at an early stage (Rizk et al., 2020). In addition, a broad range of NDE methods, including infrared thermography, radiographic testing, acoustic emission, microwave and terahertz techniques, as well as electromagnetic and ultrasonic testing, have been studied for various inspection and monitoring purposes (Hellstein and Szwedo, 2016; Fantidis et al., 2011; Zhong, 2019; Wang et al., 2018).

Several key limitations hinder the widespread field deployment of these NDE techniques. First, many optical and laser-based systems are constrained by limited operational range and require complex, time-consuming setup procedures (Poozesh et al., 2016). Second, an inherent trade-off exists between spatial resolution and acquisition speed when scanning large structures such as utility-scale wind turbine blades: high-resolution measurements require prolonged scanning times, whereas faster acquisitions often compromise defect detectability. Third, some techniques exhibit strong sensitivity to environmental interference. For example, camera-based systems require sufficient illumination to reliably track surface markers, often necessitating artificial lighting or reflective targets during nighttime inspections, thereby increasing deployment complexity in field environments.

https://doi.org/10.5194/wes-2026-104
Preprint. Discussion started: 3 July 2026

eawe european academy of wind energy
Open Access WIND ENERGY SCIENCE DISCUSSIONS

The recent emergence of robust and cost-effective automotive lidar systems with camera-level resolution presents significant opportunities for wind energy applications beyond their conventional roles in navigation and autonomous driving. It is important to distinguish these systems from Doppler wind lidars, which are widely used in wind energy for remote sensing of wind resources. Doppler lidars determine wind speed and direction by measuring the frequency shift of laser light backscattered by atmospheric aerosols or particles (Abari et al., 2014; Jin et al., 2022, 2023). In contrast, automotive-grade lidars are fundamentally range-finding devices that operate by emitting laser pulses and measuring the round-trip time of the reflected signal. Using the speed of light and the refractive index of the propagation medium, this time-of-flight principle enables precise distance estimation (Abir et al., 2023). Owing to their high spatial resolution, long operational range, and decreasing cost, these sensors are increasingly employed in applications such as topographic mapping, object detection, and structural inspection, thereby highlighting their potential for structural monitoring in the wind energy sector.

Motivated by these capabilities, the present study investigates the feasibility of commercial 3D automotive lidar systems for measuring the structural dynamics of blades on a mid-scale onshore wind turbine. The proposed sensing approach leverages the compact form factor, cost-effectiveness, high measurement precision, and long operational range of these sensors. Unlike conventional embedded sensing systems, automotive lidars provide direct measurements of blade deflection (in meters) and pitch angle (in degrees), eliminating the need for complex calibration procedures. Building on these advantages, a novel monitoring architecture is proposed in which three lidar sensors are mounted on the spinner, each co-rotating with an individual turbine blade. This configuration enables simultaneous, full-scale deformation measurements of all three blades under varying outdoor operating conditions. Furthermore, the proposed system offers strong potential for real-time structural monitoring. Combined with advanced pitch control strategies, direct lidar-based deformation measurements could improve power generation, reduce the risk of blade–tower collisions, and enhance overall operational safety.

The remainder of this paper is organized as follows. Section 2 introduces the measurement campaign. Section 3 describes the methodology used to quantify blade flapwise deflection and torsional deformation. Section 4 presents the results and corresponding analysis. Finally, Section 5 summarizes the main findings and outlines directions for future work.

2 Measurement Campaign

2.1 Site description

The measurement campaign was conducted at the Risø campus of the Technical University of Denmark (DTU). The examined turbine is the DTU Vestas V52 wind turbine, located 120.3 m from a meteorological mast (met mast) at an orientation of 20° south of east, as shown in Figure 2. The turbine has a rotor diameter of 52 m and a hub height of 44 m, with a nominal power output of 850 kW. A summary of its key characteristics is provided in Table 1.

It is worth noting that the DTU Vestas V52 wind turbine was operated at a customized rated power of 750 kW in this study, corresponding to a rated wind speed of 12 $\mathrm{m/s}$. This operating condition was identified through analysis of SCADA data, with the selected periods further restricted to predominantly westerly wind conditions.

https://doi.org/10.5194/wes-2026-104
Preprint. Discussion started: 3 July 2026

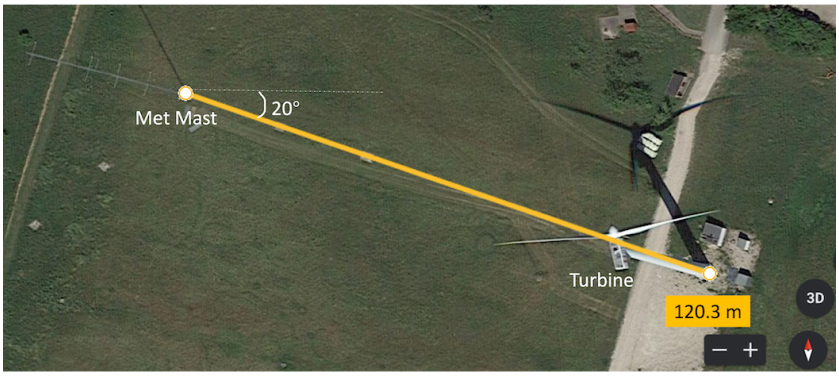

Figure 2. Top view of the experiment field at DTU Risø Campus. The DTU Vestas V52 wind turbine is located 120.3 m towards the southeast of a meteorological mast (picture © 2022 Google Earth).

Table 1. Key characteristics of the DTU Vestas V52 wind turbine.

Technical parameter	Data
Cut-in wind speed	4 m/s
Cut-out wind speed	25 m/s
Number of blades	3
Rated rotor speed	26 rpm
Tilt angle	6°
Blade coning angle	3°
Blade length	25.3 m
Twist blade root / tip	16° / 0°
Chord width root / tip	2.3 m (max) / 0.33 m
Orientation and rotation	Upwind, clockwise (front view)

The met mast instrumentation comprises five sonic anemometers (USA-1, Metek) and five cup anemometers (P2546A from WindSensor). The instruments are mounted at heights of 18 m, 31 m, 44 m, 57 m, and 70 m above ground level, with each sonic anemometer paired with a cup anemometer mounted on an opposing boom. The sonic anemometers recorded data at a sampling frequency of 50 Hz. In the present study, the anemometers located at 18 m, 44 m and 70 m were used to characterize the flow conditions at the rotor bottom, hub height, and rotor top, respectively.

2.2 Instrumentation

The Livox Avia (Livox Tech, 2025), a commercial automotive-grade lidar, was selected for this investigation. The sensor offers both repetitive and non-repetitive scanning modes. In repetitive line-scanning mode, it provides a field of view (FOV) of 70.4° × 4.5°/ 6.8° with a scan repetition cycle of 0.1 s, making it well suited for measuring high-frequency blade deflections, as

https://doi.org/10.5194/wes-2026-104
Preprint. Discussion started: 3 July 2026

illustrated in Figure 3. Additional key attributes of this sensor include a compact form factor (498 g), relatively low cost (1445 euros), high measurement precision (2 cm), and robust long-range performance up to 320 m for targets with infrared reflectivity of at least 80%.

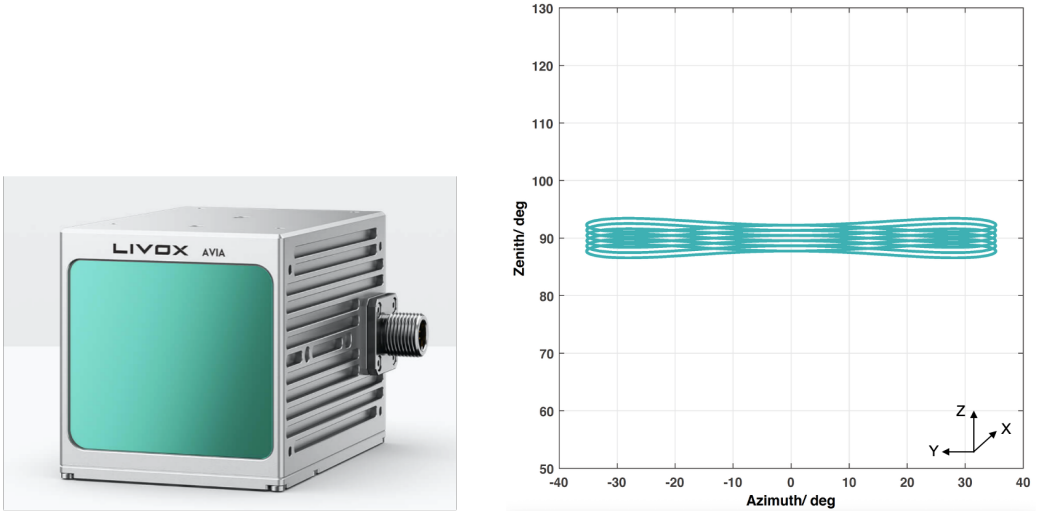

(a) (b)

Figure 3. Livox Avia 3D lidar (picture © Livox): (a) Avia with compact dimensions of 9.1 cm × 7.5 cm × 6.5 cm; (b) Repetitive scanning point cloud pattern.

In the proposed configuration, three Avia lidars were mounted on a 3.2 m boom installed at the center of the DTU Vestas V52 wind turbine spinner (Figure 4). The boom extended 2.5 m outside the spinner, while the remaining 0.7 m was securely clamped within the spinner to ensure structural stability. To adequately capture the blade tips, each lidar sensor was oriented at approximately 57° relative to the boom centerline, with each sensor dedicated to independently scanning a single blade. This configuration ensures that the lidar sensors co-rotate with the spinner, thereby eliminating relative rotational motion between the lidars and the blades; however, the lidar sensors do not pitch with the blades.

The boom was stabilized using guy wires and supported an external GPS antenna at its outer end. Serving as a common timing reference, the antenna enabled precise synchronization of the real-time point clouds from the three lidar sensors and facilitated temporal alignment with measurements from other instruments for subsequent data comparison. Timestamp analysis confirmed synchronization accuracy within 1 ms across all three units. Data acquisition was performed by an on-board computer housed inside the spinner. Equipped with 2 TB of storage, the system continuously recorded the high-rate data stream, corresponding to approximately 240,000 points per second for each individual lidar sensor.

Following turbine shutdown under low wind speed conditions, the reference positions of the stationary blades were measured using a Leica total station (Leica Geosystems, last access: 10 June 2026.) to establish a geometric baseline. With a point spacing of about 1 cm, the scan provided sufficient resolution to capture the detailed blade geometry, as depicted in Figure 5. Simultaneously, the three Livox lidar units scanned the same stationary configuration, providing the data necessary to align the

https://doi.org/10.5194/wes-2026-104
Preprint. Discussion started: 3 July 2026

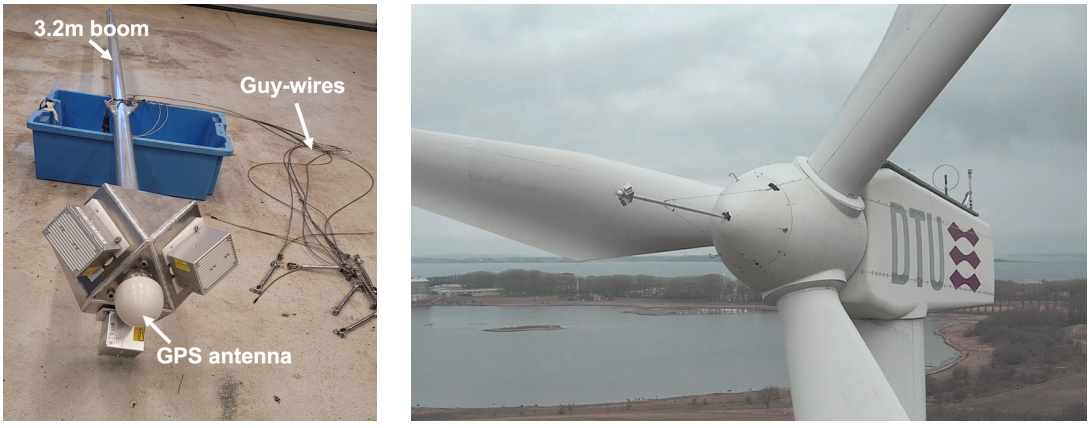

(a) (b)

Figure 4. Experiment setup of the spinner-mounted monitoring system: (a) Three Livox Avia lidar sensors mounted on the aluminum boom prior to installation; (b) Close-up view of the system attached to the spinner of the DTU Vestas V52 wind turbine (photo credit: Michael Sejer Rasmussen).

lidar and Leica total station coordinate systems during post-processing. The corresponding rotation matrix is given by:

$$M = \begin{bmatrix} 1 & 0 & 0 \\ 0 & 0 & -1 \\ 0 & 1 & 0 \end{bmatrix} \cdot \begin{bmatrix} \cos\beta & \sin\beta & 0 \\ -\sin\beta & \cos\beta & 0 \\ 0 & 0 & 1 \end{bmatrix} \tag{1}$$

where β represents the orientation angle between each Livox Avia unit and the boom centerline, with values of 55.8°, 57.9°, and 57.3° for lidar units A, B, and C, respectively. The resulting alignment between the Livox and Leica point clouds for the three blades is illustrated in Figure 6.

Following baseline acquisition, continuous dynamic measurements were conducted over 10- or 15-minute intervals during turbine operation under a range of meteorological conditions, including both daytime and nighttime periods. The Livox lidar data were processed at a temporal resolution of 33.3 Hz. For each time step, a translation and rotation matrix were calculated to register the dynamic point cloud to the static reference frame; the corresponding registration methodology is described in Section 3.

3 Methodology

3.1 Blade point cloud segmentation

Consistent with cantilevered beam behavior, blade deflections increased progressively along the span, reaching a maximum at the tip. However, the 25.3 m blade of the DTU Vestas V52 turbine exhibits relatively high structural stiffness compared with the more flexible blades used in modern large-scale wind turbines. For the analysis, the blade span from 2 m root cutoff to the

https://doi.org/10.5194/wes-2026-104
Preprint. Discussion started: 3 July 2026

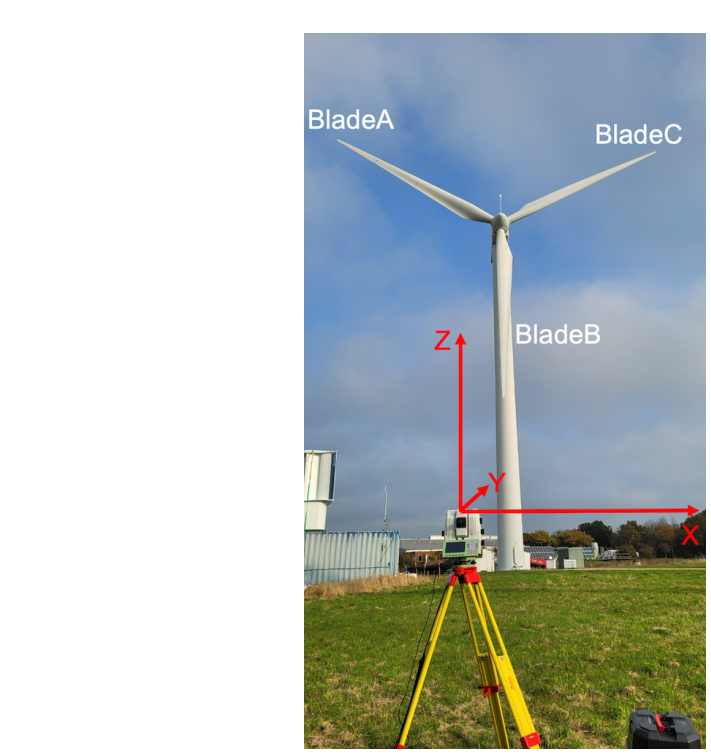

(a)

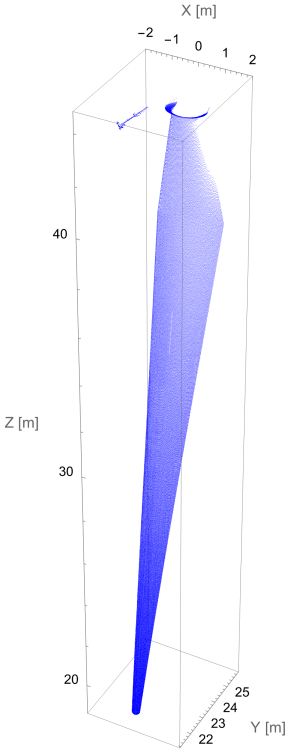

(b)

Figure 5. Establishment of the geometric baseline using stationary blade scans: (a) Leica total station setup for blade geometry acquisition, with blades labeled A, B, and C; (b) High-resolution reference point cloud with approximately 1 cm point spacing used for lidar coordinate alignment.

tip was divided into eight consecutive segments, as shown in Figure 7. The segmentation was defined using a reference vector extending from the rotor center through the root cylinder to the blade tip.

The six proximal segments were each 3 m in length, followed by a 2 m segment near the blade tip and a final 4 m tip segment. The increased length of the outermost segment compensates for the reduced spatial point density resulting from the blade's tapered geometry and the long measurement distance from the lidar sensor. Deflection and pitch angle were subsequently computed at the centroid of each segment, thereby providing spatially resolved measurements along the blade span.

3.2 Quantification of blade deflection and pitch angle

Quantification of blade deflection and pitch angle for each segment was achieved by registering the Livox point cloud (red points in Figure 7) to the stationary reference points (black points). A rigid-body transformation with five degrees of freedom, comprising translations $\{x, y, 0\}$ and rotations $\{\mathrm{roll}(x), \mathrm{pitch}(y), \mathrm{yaw}(z)\}$, was applied at the centroid of each segment. The optimal transformation parameters were determined using the Amoeba optimization algorithm, also known as the Nelder–

https://doi.org/10.5194/wes-2026-104
Preprint. Discussion started: 3 July 2026

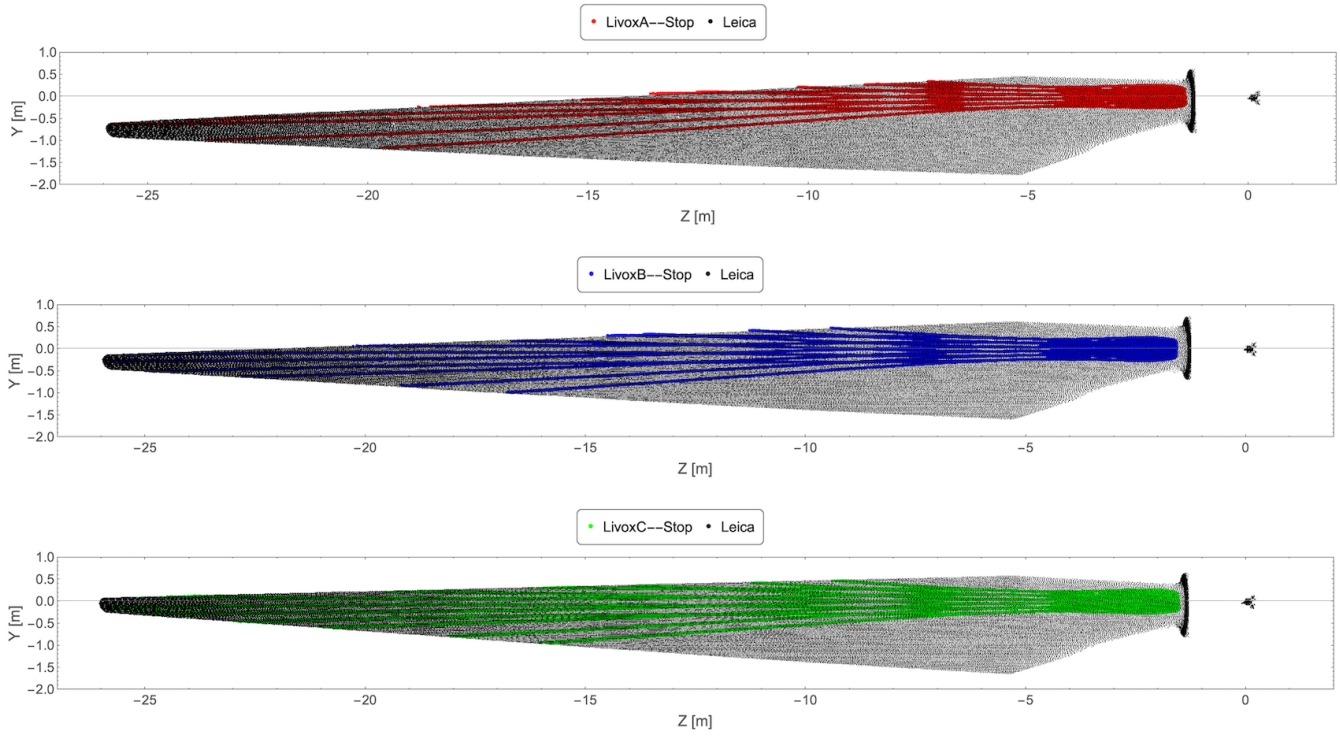

Figure 6. Alignment of stationary blade point clouds acquired by Livox Avia lidar sensors and the Leica total station after application of the rotation matrix.

Mead downhill simplex method (Nelder, 1965). This optimization technique performs multidimensional function minimization through iterative simplex transformations. Although computationally less efficient than gradient-based approaches, the algorithm is widely used because of its simplicity and robustness. Currently, extracting the point cloud from a 1-second Livox data file and computing the transformation matrices for all eight segments requires approximately 10 seconds of processing time. However. this computational cost could be substantially reduced through optimized data processing, dedicated computational resources, and automated analysis pipelines.

Within this framework, the translation parameters are interpreted as follows: x denotes flapwise deflection, defined as displacement along the x-axis (positive toward the tower), while y corresponds to edgewise deflection, defined as displacement along the y-axis (positive in the direction of rotation). The rotational parameter corresponding to yaw about the z-axis (positive upward), defines the pitch angle of each blade segment.

Although three Livox Avia lidars were deployed to simultaneously capture the motion of all three blades, validation against strain gauge measurements and SCADA data is presented only for Blade C. This choice was motivated by two considerations. First, strain gauge data for Blades A and B were unavailable during the measurement campaign. Second, the DTU Vestas V52 turbine employs collective pitch control, in which all three blades are pitched simultaneously by the same angle (Behera and

https://doi.org/10.5194/wes-2026-104
Preprint. Discussion started: 3 July 2026

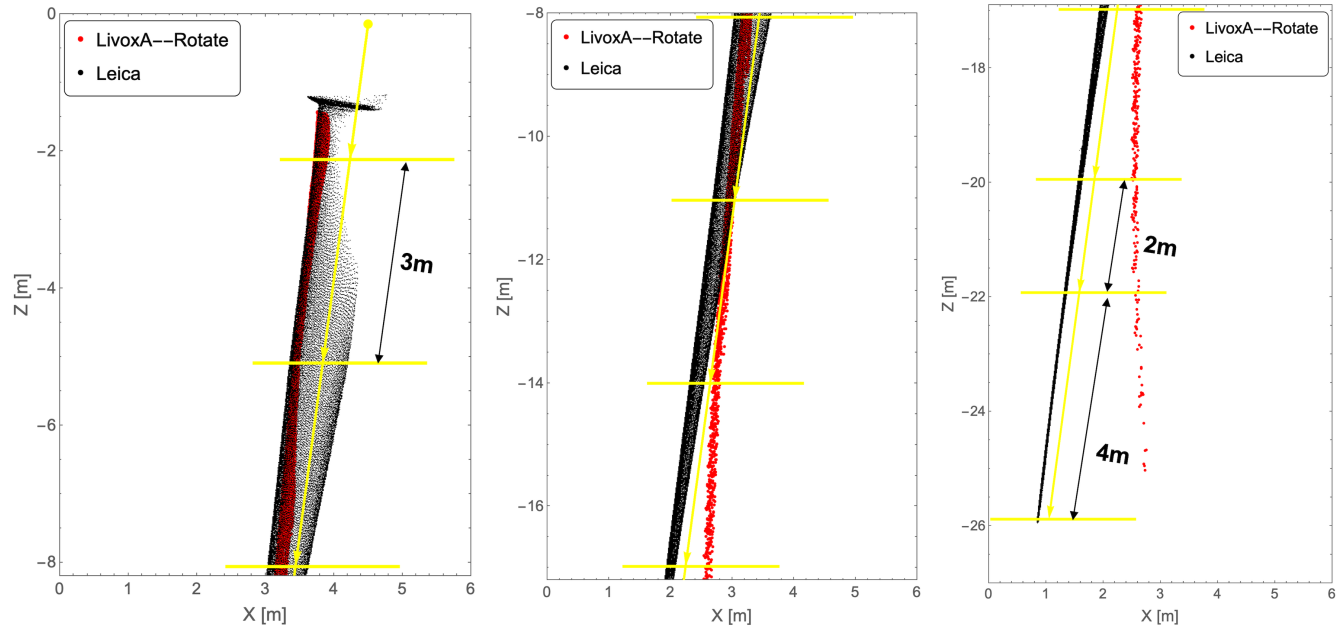

Figure 7. Segmentation of the DTU Vestas V52 Blade A into eight spanwise segments for deflection and pitch angle analysis at segment centroids. Black: stationary reference scan (Leica); Red: dynamic scan (Livox) during turbine rotation.

Gambier, 2018). Therefore, the SCADA-derived pitch signal is identical for all blades. Blade C was consequently selected as the representative case for validating the lidar-derived measurements against both strain gauge and SCADA data.

4 Results and Discussion

4.1 Validation of lidar-derived flapwise deflection measurements

The present study examines nine operational cases, each based on 10- or 15-minute measurement intervals collected between March and July 2025. Table 2 summarizes the corresponding mean wind speeds, wind directions, and shear exponents for each case. These meteorological parameters were derived from sonic anemometer measurements obtained from the nearby meteorological mast, as described in Section 2.

Among the nine cases, four correspond to below-rated wind conditions with mean wind speeds well below the rated wind speed of 12 $\mathrm{m/s}$, three represent near-rated conditions, and the remaining two correspond to above-rated operation. The wind shear exponent was defined as $\alpha = d\ln U / d\ln z$, where U denotes wind speed and z is height above ground level. For each case, α was estimated using wind speed measurements from sonic anemometers installed at 18 m and 70 m, representing the lower and upper bounds of the rotor-swept area, respectively.

https://doi.org/10.5194/wes-2026-104
Preprint. Discussion started: 3 July 2026

eawe european academy of wind energy
Open Access WIND ENERGY SCIENCE DISCUSSIONS

Table 2. Meteorological conditions for the nine measurement cases, with mean wind speed at hub height (44 m), wind direction at the upper rotor plane (70 m), wind shear, and turbulence intensity (TI).

Date	Mean wind speed (m/s)	Wind direction (°)	Shear exponent (-)	TI (-)	Rated?
2025-03-22	9.5	87	0.38	0.25	Below rated
2025-03-28	6.4	201	0.12	0.16	Below rated
2025-04-10	15.8	293	0.06	0.09	Above rated
2025-04-15	9.1	91	0.28	0.31	Below rated
2025-05-15	11.0	341	0.18	0.14	Near rated
2025-05-15	10.4	334	0.16	0.16	Near rated
2025-05-27	5.6	220	0.17	0.19	Below rated
2025-06-29	12.0	224	-	0.13	Near rated
2025-07-03	13.0	217	-	0.11	Above rated

For wind directions within the sector of 73° to 150°, the met mast is positioned downstream of the turbine and therefore lies within its wake (Yankova and Kock, 2018). This introduces a velocity deficit at the mast location, resulting in a biased shear exponent for the measurements on 2025-03-22 and 2025-04-15 relative to the undisturbed atmospheric shear. The remaining seven cases are characterized by westerly wind conditions, during which the mast is free from wake effects. On 2025-06-29 and 2025-07-03, wind speed data at the key measurement heights were unavailable. Consequently, shear exponents could not be calculated and are denoted as 0 in the relevant figures and tables.

During post-processing, the root segment exhibited a small but non-negligible sinusoidal deflection pattern (Jin and Mann, 2026). This motion is attributed to elastic deformation of the boom caused by the combined mass of the aluminum mounting heads and the three Livox lidar units. From the centroid position and deflection amplitude of the root segment, the boom bending angle was estimated to range between 1.0° and 1.4° across the nine measurement cases, with higher values observed at higher wind speeds.

Given the relatively high stiffness of the DTU Vestas V52 blade, flapwise deflection at the root segment is assumed to be negligible. Consequently, the observed root motion is interpreted as arising solely from boom bending and vibration rather than true blade deformation. This motion introduces a systematic bias that propagates along the blade, with an estimated boom angle of 1.0° corresponding to an apparent flapwise deflection of approximately 0.4 m at the blade tip. To correct for this effect, the boom-induced contribution was removed by scaling the root segment deflection according to the centroid position ratio of each segment relative to the root. This correction ensures that the reported flapwise deflections reflect true blade behavior rather than superimposed structural motion of the support system, which is essential for obtaining physically meaningful results.

In accordance with cantilevered beam theory, tip deflection and root bending moment describe the same underlying physical phenomenon. However, these quantities are expressed in different units, namely deflection in meters from the Livox lidar measurements and bending moment in mV/V from the strain gauges. To enable direct comparison, both signals, the boom-

https://doi.org/10.5194/wes-2026-104
Preprint. Discussion started: 3 July 2026

corrected lidar deflection and the strain gauge measurements, were normalized to dimensionless form, removing dependence on their original units. The comparison specifically examines the tip segment flapwise deflection, computed at its centroid located 23.8 m from the rotor center with a sampling frequency of 33.3 Hz, against the bending moment measured by the strain gauge embedded at 1.4 m from the rotor center with a sampling frequency of 50 Hz.

Figure 8 presents this comparison for five representative operational cases, covering a mean hub-height wind speed range of 5.6 $\mathrm{m/s}$ to 15.8 $\mathrm{m/s}$. These cases are selected to illustrate the agreement across the full operating envelope, including conditions below-, near-, at-, and above-rated wind speed. The corresponding comparisons for the remaining four cases are provided in Figure A1. Across all cases, the lidar-derived flapwise deflection shows close agreement with the strain gauge measurements, reproducing both the amplitude and temporal variation of the blade response. This consistency across a wide range of wind and operating conditions demonstrates the capability of the Livox Avia lidar system to accurately measure flapwise blade deflection.

Spectral analysis of flapwise deflection further confirms the agreement between the Livox Avia lidar and strain gauge measurements. As illustrated in Figure 9 and Figure A2, the two datasets exhibit consistent spectral characteristics, with matching peak positions and comparable amplitudes across the frequency domain for all cases, thereby reinforcing the validity of the lidar-based approach. At the lowest mean wind speed of 5.6 $\mathrm{m/s}$, the spectrum is dominated by a single distinct peak at the fundamental rotational frequency (1P), corresponding to 0.28 Hz due to the slower rotor speed under low wind conditions. As wind speed increases to at- and above-rated levels (Figure 9 (c)-(e)), higher-order harmonics up to 5P or 6P become increasingly prominent. Concurrently, rotor speed regulation maintains the 1P frequency at a approximately 0.44 Hz across these operating regimes. This corresponds to the rated rotor speed of 26 rpm, yielding a fundamental rotational frequency of 0.44 Hz (i.e., 26 rpm / 60 s).

A notable feature is observed for 2025-07-03, with a mean hub-height wind speed of 13 $\mathrm{m/s}$, where higher harmonics extend up to 8P. This behavior may be associated with transient resonance conditions arising from the interaction between rotational harmonics and structural natural frequencies. The effect may also be influenced by controller dynamics or specific inflow conditions on that day, highlighting the complex coupling between aerodynamic loading and structural response in operational wind turbines.

4.2 Dependence of median flapwise deflection on mean wind speed

All measurement cases were acquired over durations of approximately 10 to 15 minutes. Figure 10 presents the median flapwise deflection for each measurement period as a function of mean hub-height wind speed for the eight spanwise segments. Given the relatively small rotor diameter of the turbine, the mean wind speed at hub height exhibits limited variation compared to that at the rotor top and bottom, even when the shear profile is considered. In a simplified cantilever beam model, the flapwise deflection is approximately proportional to the aerodynamic loading. However, the aerodynamic load (F_{load}) is not linearly proportional to the mean hub-height wind speed (U_{hub}); instead, it can be expressed as:

$$F_{load} \propto U_{hub}^2 C_T$$

https://doi.org/10.5194/wes-2026-104
Preprint. Discussion started: 3 July 2026

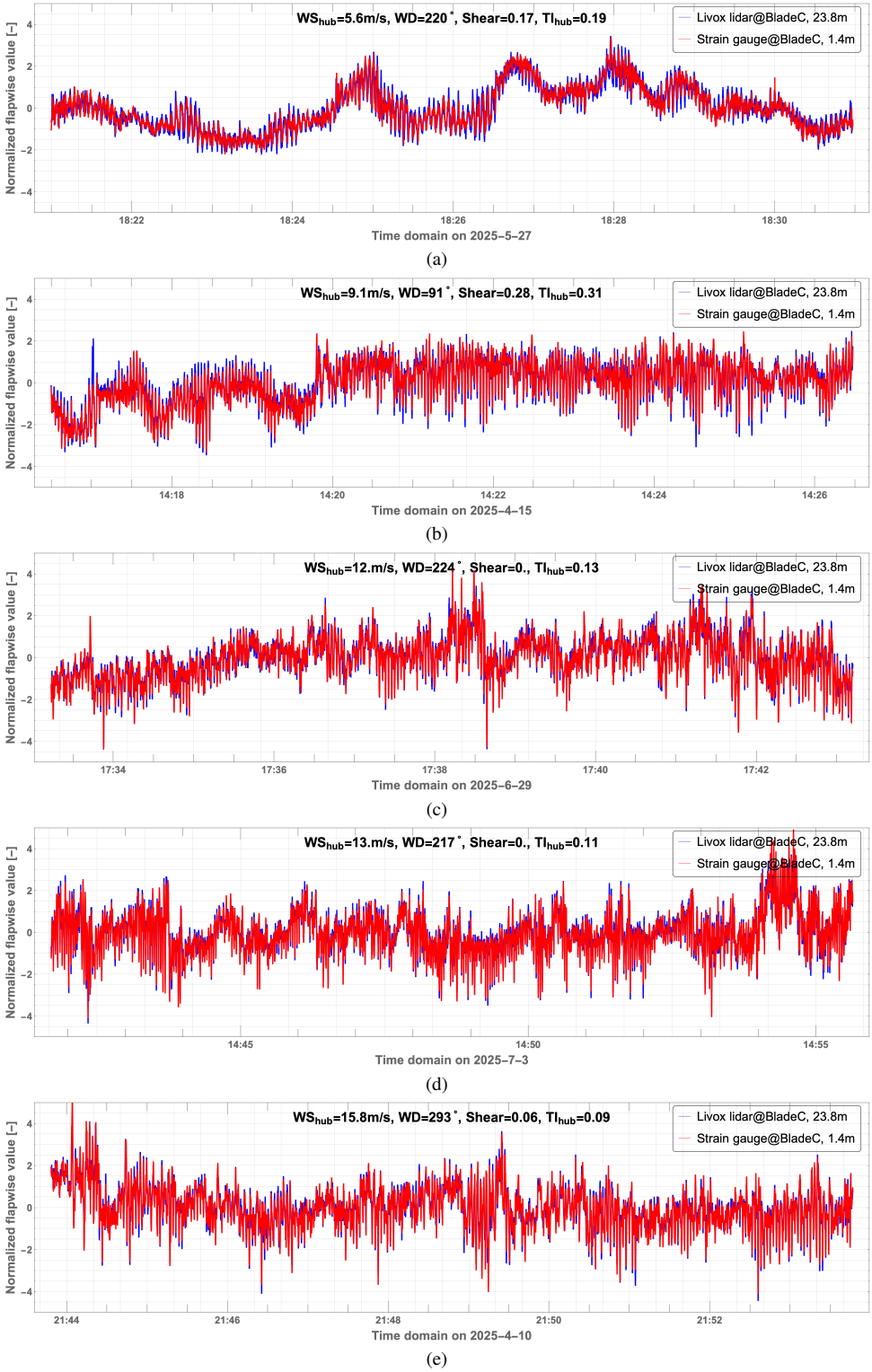

Figure 8. Normalized flapwise deflection validation: Livox lidar vs. strain gauge bending moments under different wind conditions.

https://doi.org/10.5194/wes-2026-104
Preprint. Discussion started: 3 July 2026

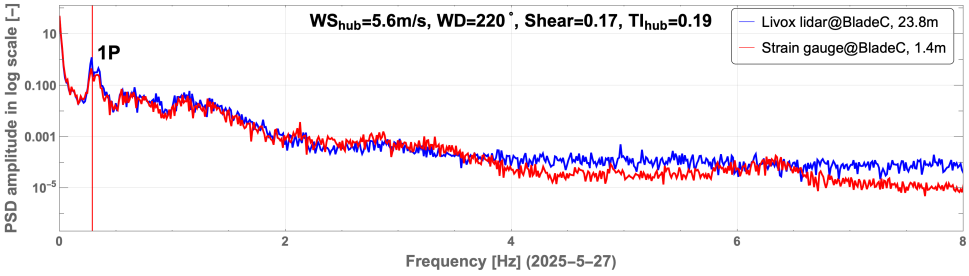

(a)

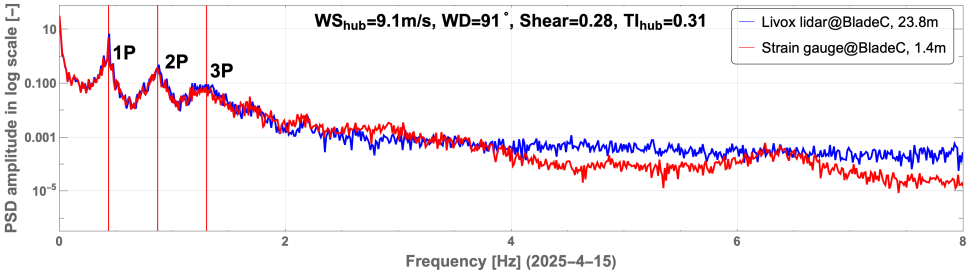

(b)

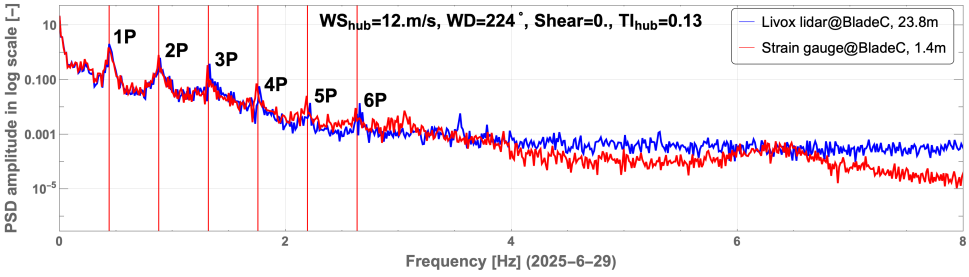

(c)

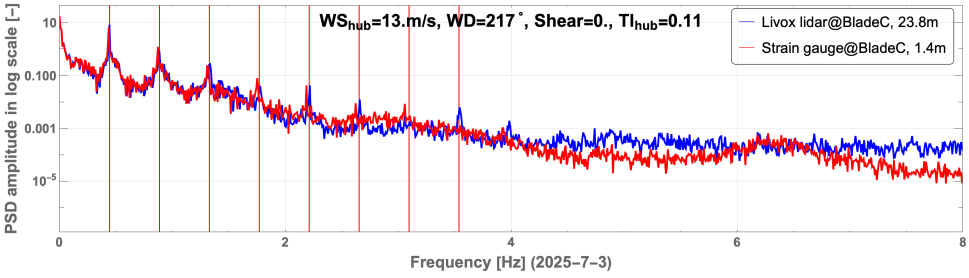

(d)

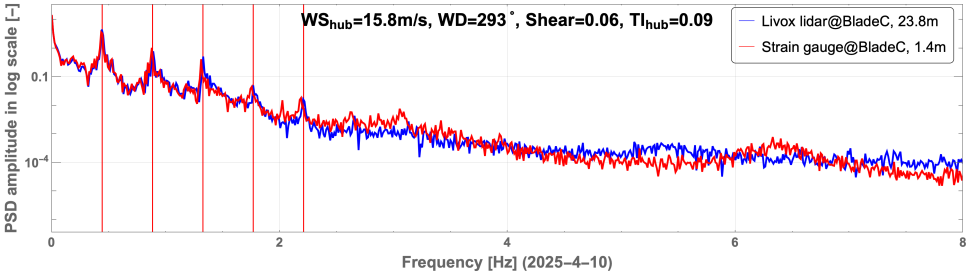

(e)

Figure 9. Spectral validation of normalized flapwise deflection: Livox lidar vs. strain gauge data under different wind conditions.

https://doi.org/10.5194/wes-2026-104
Preprint. Discussion started: 3 July 2026

eawe european academy of wind energy
Open Access WIND ENERGY SCIENCE DISCUSSIONS

where C_T is the thrust coefficient, which depends on blade design, pitch angle, and rotor speed. For the three tip-adjacent segments at radial positions of 18.4 m, 20.8 m, and 23.8 m (Figure 10 (a)), the curves clearly delineate the distinct operational regimes of the blade. Below the rated wind speed of 12 m/s, flapwise deflection increases with increasing wind speed. Although a quadratic dependence on wind speed is expected in theory, the observed relationship deviates from a perfect parabolic trend.

At rated wind speed, the maximum thrust force is typically attained. In the present measurements, however, peak deflection occurs at approximately 11 m/s, slightly below the rated condition. A possible explanation is that the mean wind speed represents a temporal average over the 10 to 15 minute measurement interval. Consequently, a mean value of 11 m/s may include instantaneous wind speeds reaching or exceeding the rated threshold of 12 m/s. Above rated wind speed, blade pitch control reduces the effective aerodynamic loading to maintain constant power output, leading to a reduction in flapwise deflection.

For the inner blade sections, specifically from the root to 9.4 m, the cross-section is nearly cylindrical and therefore less affected by pitch regulation. As shown by the lower curves in Figure 10 (a), median flapwise deflection in these segments increases monotonically with increasing mean wind speed. However, a more detailed interpretation of this behavior requires further investigation through numerical modeling.

Consistent with the segment-wise results in Figure 10 (a), the full-scale blade response shown in Figure 10 (b) exhibits similar dependence on mean wind speed. Under above-rated operating conditions (wind speeds exceeding 12 m/s), the dashed curves indicate that flapwise bending in the blade tip region decreases with increasing wind speed due to pitch regulation, whereas deflection in the root region shows a slight increase compared with lower wind speed cases.

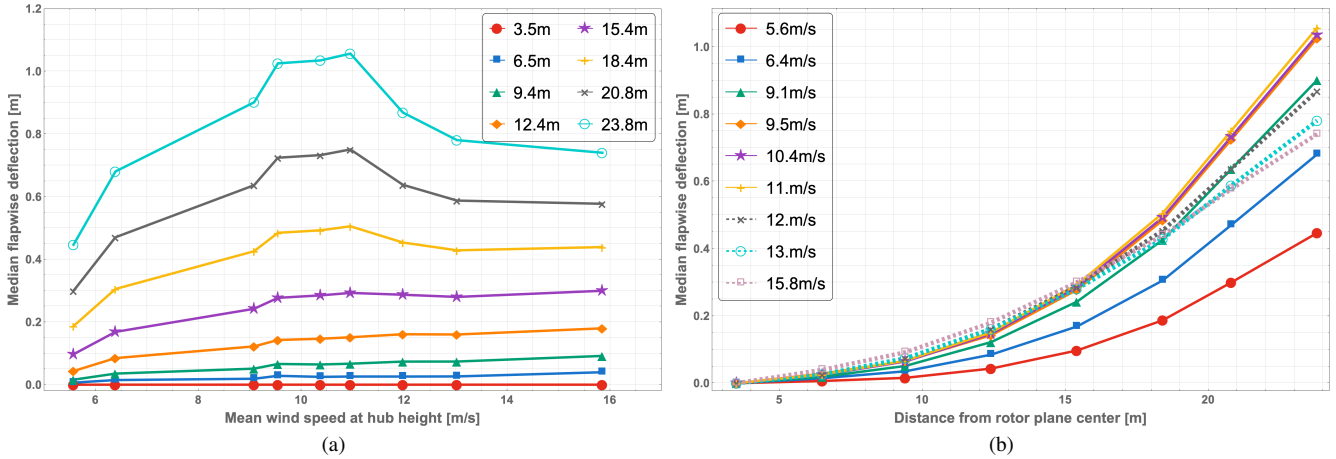

Figure 10. Relationship between median flapwise deflection and mean hub-height wind speed for each measurement period: (a) Segment-wise blade response; (b) Integrated full-scale blade response.

https://doi.org/10.5194/wes-2026-104
Preprint. Discussion started: 3 July 2026

eawe european academy of wind energy
Open Access WIND ENERGY SCIENCE DISCUSSIONS

4.3 Dependence of median flapwise deflection on rotor azimuth angle

During turbine rotation, the tower is scanned each time a blade passes. These scans are recorded using high-accuracy timestamps synchronized to the external GPS, thereby providing a temporal reference that corresponding to a rotor azimuth angle of 180°, i.e., when the blade is directly in front of the tower. Using this reference timestamp, flapwise deflection at other azimuthal positions can be interpolated. Figure 11 presents the resulting relationship between median flapwise deflection and rotor azimuth angle, with the vertical green line indicating the reference position at 180°. For all nine measurement cases, flapwise deflection attains its maximum near the rotor plane top (approximately 0°) and its minimum near the rotor plane bottom (approximately between 200° and 220°).

Several factors may influence the observed azimuthal variation, including blade gravity, wind speed, wind shear, and yaw misalignment. Wind shear is expected to play a particularly important role, especially for large wind turbines. Except for the two cases on 2025-06-29 and 2025-07-03, for which shear data were unavailable, all measurement cases exhibit positive shear exponents. Under positive wind shear, the highest wind speed occurs near the rotor top position (0°), leading to increased aerodynamic loading and consequently larger flapwise deflection. As the blade approaches the tower-crossing position at 180°, both wind speed and aerodynamic loading decrease.

This reduction is further enhanced by the tower-induced stagnation effect upstream of the tower, which typically extends over several degrees of azimuth rotation. During this interval, the tower partially blocks the incoming airflow, inducing a localized reduction in wind speed and a corresponding temporary drop in aerodynamic loads (Noyes et al., 2018). The combined effect manifests as a brief but distinct reduction in flapwise deflection near the tower-crossing position.

Gravity does not directly contribute to flapwise deflection in a perfectly aligned rotor. However, rotor tilt and blade coning introduces a small gravitational component in the flapwise direction. Additionally, structural coupling may allow edgewise blade motion to contribute indirectly to flapwise deformation.

Under ideal conditions with positive wind shear, the maximum flapwise deflection would be expected near the rotor top (0°), while the minimum would occur at the tower-crossing position (180°), resulting in a symmetric azimuthal distribution. However, the measured curves in Figure 11 exhibit clear asymmetry. As indicated by the vertical and horizontal green reference lines, both extrema display a phase lag relative to the idealized positions, with a more pronounced delay observed near the rotor-bottom position.

This asymmetry can primarily be attributed to blade inertia and unsteady aerodynamic effects. Blade inertia induces a phase lag between the applied aerodynamic loading and structural response, thereby shifting the deflection extrema away from their idealized azimuthal locations. Furthermore, aerodynamic forces do not respond instantaneously to changes in angle of attack, but instead develop over a finite time scale. This behavior can be interpreted within the framework of unsteady aerodynamics through the Theodorsen function (Fung, 2008), which characterizes the phase relationship between angle-of-attack variations and the delayed aerodynamic forcing. According to this theory, the associated phase lag between angle is approximately 4°, further contributing to the observed asymmetry.

https://doi.org/10.5194/wes-2026-104
Preprint. Discussion started: 3 July 2026

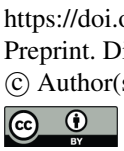

eawe european academy of wind energy
Open Access WIND ENERGY SCIENCE DISCUSSIONS

To quantify the phase delay, sinusoidal functions was fitted to the measured deflection curves. However, due to complex inflow conditions and aeroelastic coupling between blade motion and aerodynamic loading, the fitted phase delay is prone to overestimation, reaching values as high as 51°. The actual phase shift is therefore expected to lie within a range of 10° to 40° relative to the symmetric reference position at 180°.

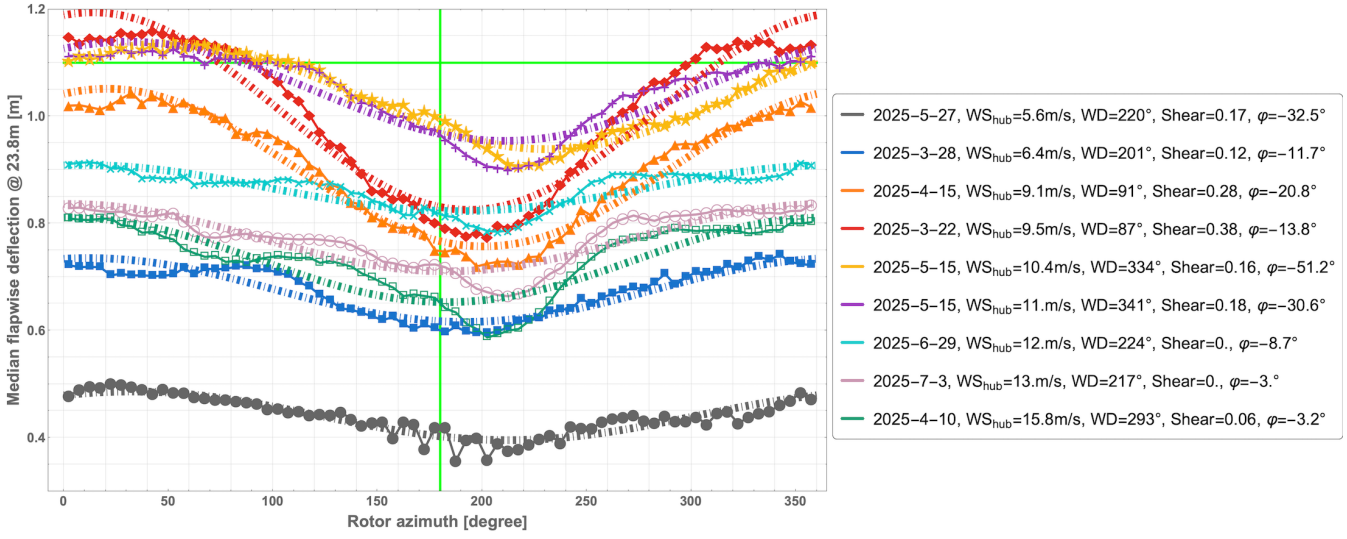

Figure 11. Relationship between median flapwise deflection and rotor azimuth angle under various wind conditions, including fitted phase lag induced by blade inertia and variations in aerodynamic loading.

It is also of interest to evaluate the peak-to-peak amplitude, defined as the difference between the maximum and minimum flapwise deflection, to assess whether wind speed or shear exponent exerts a stronger influence on this metric. The results are presented in Figure 12. Along the blade span, both parameters have an increasingly pronounced effect toward the blade tip. Overall, however, wind shear appears to have a stronger influence than mean wind speed. This is evident from the light pink and light blue curves, which correspond to the highest shear exponents and exhibit the largest peak-to-peak amplitudes near the blade tip, despite the corresponding shear estimates being affected by the turbine wake effects. A comparison between the purple curve (mean wind speed of 10.4 $\mathrm{m/s}$, shear exponent of 0.16) and the green curve (mean wind speed of 15.8 $\mathrm{m/s}$, shear exponent of 0.06) further highlights this trend. Although the purple case exhibits a lower mean wind speed, its higher shear exponent results in a larger peak-to-peak flapwise deflection than the green case.

However, the findings presented in this section are based exclusively on measurement data. Further validation through numerical simulations and an expanded dataset spanning a broader range of wind speeds and shear conditions are therefore required.

https://doi.org/10.5194/wes-2026-104
Preprint. Discussion started: 3 July 2026

eawe european academy of wind energy
Open Access WIND ENERGY SCIENCE DISCUSSIONS

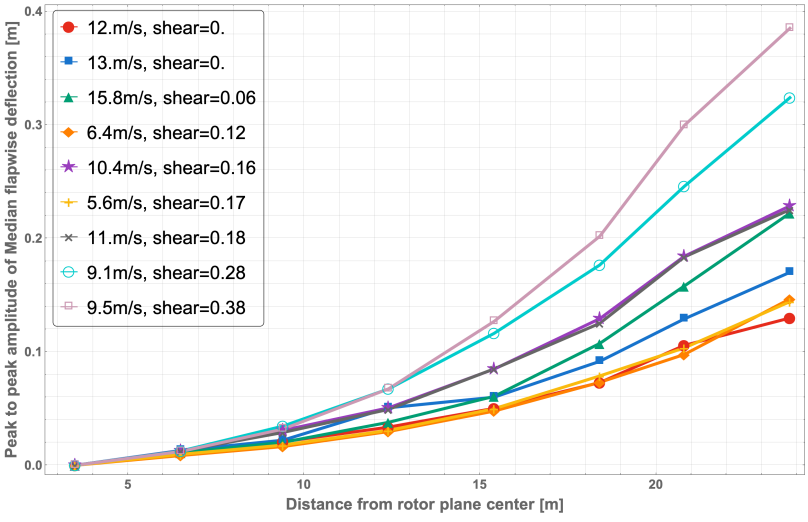

Figure 12. Peak-to-peak flapwise deflection as a function of spanwise position for nine cases spanning a range of wind speeds and shear exponents. Symbols in the legend are sorted according to shear.

4.4 Validation of lidar-derived pitch angle measurements

In addition to flapwise deflection, blade pitch angle was evaluated using measurements from the SCADA system. Because the lidar units are mounted on the turbine spinner, they co-rotate with the rotor but do not pitch with the individual blades. Consequently, the lidar-derived pitch angle, defined as the yaw rotation about the z-axis in Section 3, represents a combined measure of blade pitch and torsional deformation. The tip segment may occasionally contain an insufficient number of measurement points, leading to unreliable pitch estimates and sporadic outliers. To minimize their impact, Figure 13 and B1 compare lidar-derived pitch angles at the blade tip with the corresponding SCADA pitch measurements for all nine operating cases, after resampling both datasets to 2 Hz. The original sampling frequencies of the lidar and SCADA systems were 33.3 Hz and 50 Hz, respectively.

Consistent with the flapwise deflection results, the pitch comparison demonstrates good overall agreement between the Livox lidar measurements and the SCADA data across all nine cases. Both datasets indicate that, under below-rated wind conditions, the blade pitch angle remains close to zero, with an offset of approximately -1° to -2°. As wind speed approaches or exceeds the rated value of 12 $\mathrm{m/s}$, the pitch control system becomes active, increasing the pitch angle to regulate aerodynamic loading and maintain constant power output. Under the highest wind speed condition (15.8 $\mathrm{m/s}$), the pitch angle reaches approximately 10°, as shown in Figure 13.

The lidar-derived signal closely follows the temporal variation of the SCADA pitch measurements; however, a systematic offset is consistently observed. This discrepancy is attributed to torsional deformation near the blade tip. The SCADA signal represents the pitch angle at the blade root, measured by the pitch bearing system, and therefore does not capture structural twist along the blade span. For this relatively small and stiff DTU Vestas V52 blade, the twist component is expected to be

https://doi.org/10.5194/wes-2026-104
Preprint. Discussion started: 3 July 2026

on the order of 1°, although further validation through aeroelastic modeling is required. In addition, the lidar-derived signal exhibits periodic oscillations, as evident in Figure 13 (a), which are likely associated with boom-induced vibrations. The impact of this effect on the measured pitch response is currently under investigation and will be addressed in future work.

Because the blade is partitioned into eight spanwise segments, torsional deformation can be quantified by evaluating the difference in orientation angle (pitch plus twist) between blade sections. Figure 14 presents the resulting torsional deformation as a function of mean hub-height wind speed. To improve robustness, the penultimate segment, with its centroid located approximately 20.8 m from the rotor center, was used instead of the tip segment (23.8 m) due to the presence of outliers. The results indicate that the DTU Vestas V52 blade exhibits high torsional stiffness, with negligible twist under below-rated operating conditions, as expected. However, torsional deformation increases progressively with wind speed, reaching approximately 0.8° at wind speeds close to 16 $\mathrm{m/s}$. These observations are consistent with the expected aeroelastic response of the blade and will be further validated using HAWC2 (Horizontal Axis Wind Turbine simulation Code, second generation), a simulation tool developed by DTU Wind Energy.

5 Conclusions and future work

This study demonstrates the successful application of a spinner-mounted, multi-lidar system for full-scale monitoring of wind turbine blade deformation, with particular emphasis on flapwise deflection and pitch angle, including torsional twist. A geometric baseline reference was first established from stationary blade measurements acquired under parked turbine conditions with the blade positioned in front of the tower. Based on this reference geometry, dynamic blade deformation was subsequently quantified using synchronized measurements from three Livox Avia lidars.

To capture spanwise variations in structural response, the blade was divided into eight segments. A rigid transformation with five degrees of freedom was applied to each segment to quantify flapwise deflection as well as pitch and torsional deformation. The transformation parameters were optimized using the Nelder–Mead (Amoeba) algorithm. After correcting for boom-induced motion, corresponding to an artificial flapwise tip deflection of approximately 0.4 m, the lidar-derived flapwise deflection measurements showed strong agreement with co-located strain gauge data following normalization. This agreement was consistently observed across a wide range of wind conditions in both the time and frequency domains.

The measurements further revealed a clear dependence of flapwise deflection on rotor azimuth angle. The observed azimuthal asymmetry and phase delay are attributed to the combined effects of aerodynamic loading variations, blade inertia, and unsteady aerodynamic response. In addition, the influence of mean wind speed and wind shear on flapwise deformation was systematically investigated. Below rated wind speed, flapwise deflection in the outer blade sections increased with increasing wind speed and reached a maximum near rated operation. Under above-rated conditions, deflection in the tip region decreased due to pitch regulation and the associated reduction in aerodynamic loading. In contrast, the inner blade sections near the root exhibited comparatively weak sensitivity to wind speed variations. Furthermore, larger shear exponents produced greater peak-to-peak deflection amplitudes across the rotor plane.

https://doi.org/10.5194/wes-2026-104
Preprint. Discussion started: 3 July 2026

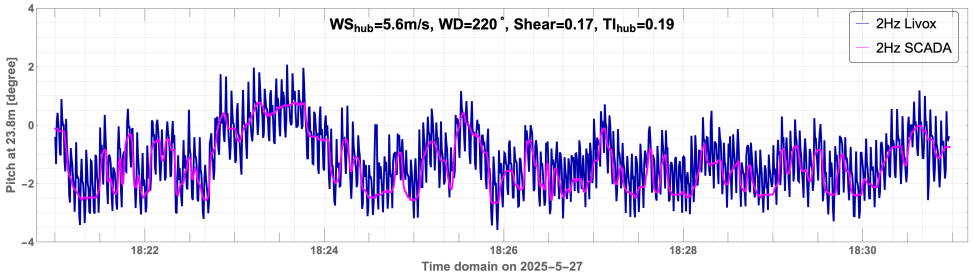

(a)

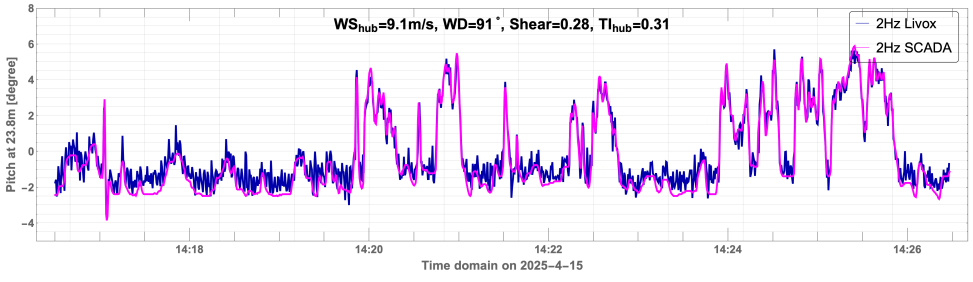

(b)

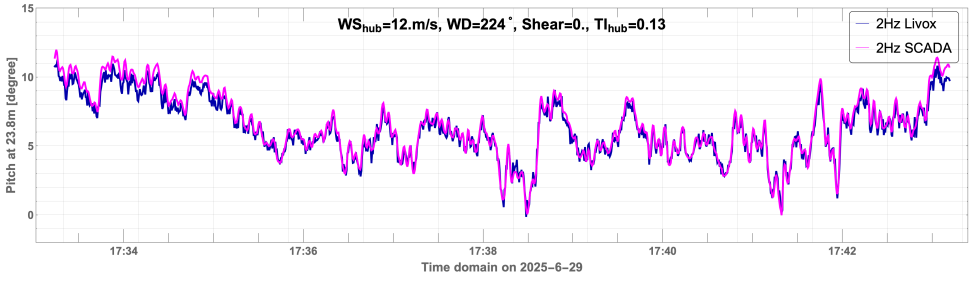

(c)

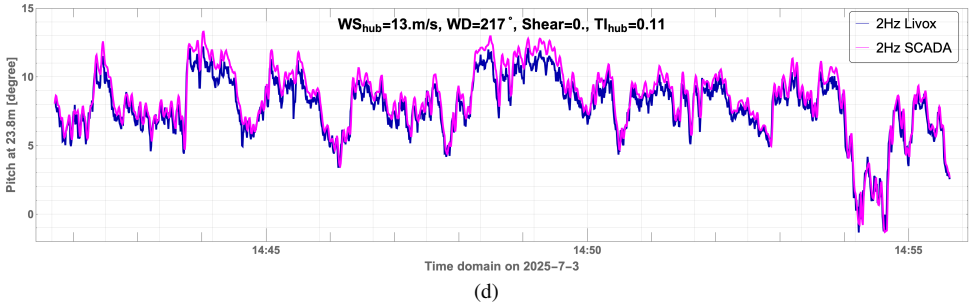

(d)

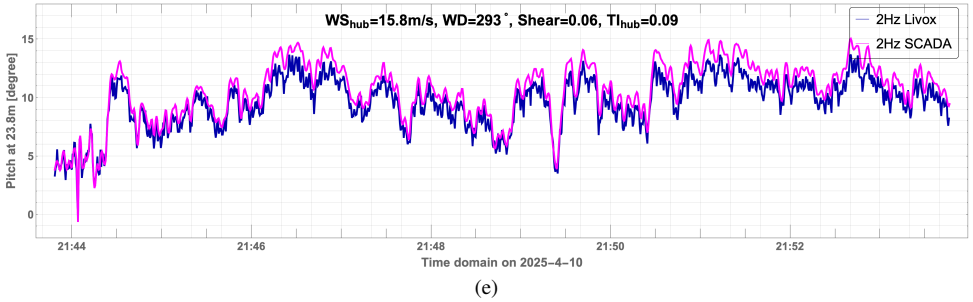

(e)

Figure 13. Comparison of 2 Hz blade pitch angle from Livox lidar measurements and SCADA data across various wind conditions.

https://doi.org/10.5194/wes-2026-104
Preprint. Discussion started: 3 July 2026

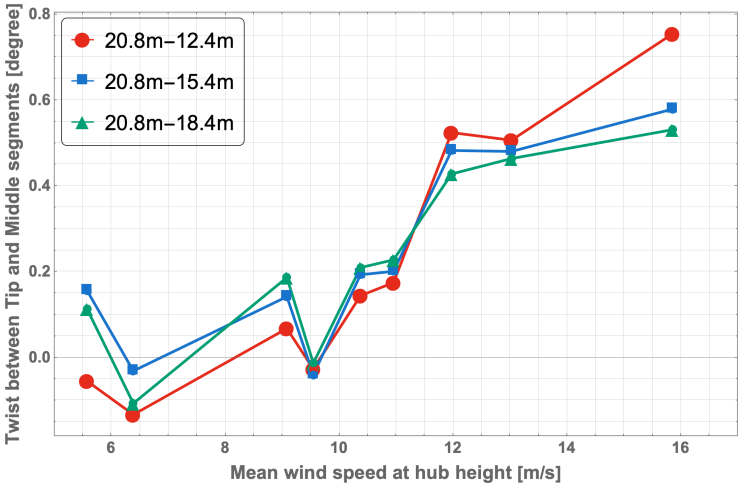

Figure 14. Torsional deformation between the mid-span and tip sections of the DTU Vestas V52 blade as a function of mean hub-height wind speed.

Good agreement was also obtained between the lidar-derived pitch measurements and the SCADA pitch signals after resampling both datasets to 2 Hz. Because the lidar system is mounted on the spinner and does not pitch with the blades, the measured signal represents a combination of blade pitch and torsional deformation that cannot be directly captured by embedded strain gauge sensors. A systematic offset between the lidar and SCADA signals was observed and attributed to blade torsional twist. By evaluating orientation differences between spanwise blade segments, torsional deformation was estimated along the blade span. The results indicate that the DTU Vestas V52 blade exhibits torsional deformation of approximately 0.8° at a mean hub-height wind speed of 16 $\mathrm{m/s}$, while torsional deformation remains negligible under below-rated operating conditions due to the relatively high blade stiffness.

Overall, the results validate the capability of cost-effective automotive lidars to provide reliable, high-resolution measurements of wind turbine structural dynamics under challenging field conditions. The adverse effects of boom bending and vibration on flapwise deflection were successfully mitigated, while ongoing work aims to further reduce their influence on lidar-derived pitch signals.

Although the proposed 3.2 m boom-mounted configuration is feasible for the DTU Vestas V52 turbine, its applicability becomes increasingly challenging for modern multi-megawatt turbines with blade lengths exceeding 80 m. In such cases, sufficiently long booms introduce substantial structural and operational challenges, particularly for offshore applications. In addition, large flapwise deflections toward the tower may reduce line-of-sight visibility of the blade tip, potentially leading to intermittent data loss in this critical measurement region.

Future work will therefore focus on alternative sensor integration architectures for large wind turbines. These include: (i) tower-mounted multi-sensor arrays to achieve full azimuthal coverage of the blade tip region; (ii) direct integration of lidar sensors within the blade structure for monitoring structural response near the blade root; and (iii) rear-mounted lidar assemblies

https://doi.org/10.5194/wes-2026-104
Preprint. Discussion started: 3 July 2026

on the spinner or individual blades, enabling direct measurement of flapwise deflection and torsional twist along the blade span. Further efforts will also include aeroelastic validation using HAWC2 simulations and expansion of the measurement dataset to adverse weather conditions, including rainfall and snow.

In parallel, the development of a dedicated software platform for synchronized data acquisition, processing, and visualization will enable a comprehensive real-time framework for wind turbine structural response monitoring. Such a system could support structural health assessment, improve operational safety, and provide high-quality experimental data for the development and validation of next-generation aeroelastic models. In addition, the proposed approach may contribute to accelerated prototype development and reduced design uncertainty without requiring proportional structural overdesign. When integrated with advanced pitch control strategies, the real-time system could also improve aerodynamic performance and enhance power production.

Data availability. The processed deflection and pitch data for all nine cases can be found by https://figshare.com/s/34e89e857b4f78be707a.

Video supplement. Two supplementary videos accompany this paper. Video 1 shows the lidar-based monitoring system installed on the spinner of the DTU Vestas V52 wind turbine (Figure 4 (b)). Video 2 presents real-time measurements from the three Livox lidars as visualized in the Livox Viewer software.

Author contributions. LJ and JM contributed to conceptualization, funding acquisition, and methodology development. LJ conducted the field experiments, performed the formal analysis, and wrote the original manuscript. JM contributed to formal analysis, and manuscript review and editing.

Competing interests. JM is a member of the editorial board of Wind Energy Science.

Financial support. This work is supported by a research grant (VIL58876) from VILLUM FONDEN.

Acknowledgements. The authors of this article express their gratitude to DTU colleagues Michael Courtney, Søren Oemann Lind, Per Hansen, Fanzhong Meng, Michael Sejer Rasmussen, Kasper Clemmensen, for their great support in this project.

https://doi.org/10.5194/wes-2026-104
Preprint. Discussion started: 3 July 2026

eawe european academy of wind energy
Open Access WIND ENERGY SCIENCE DISCUSSIONS

Appendix A: Time-domain and Spectral Comparison of Flapwise Deflection

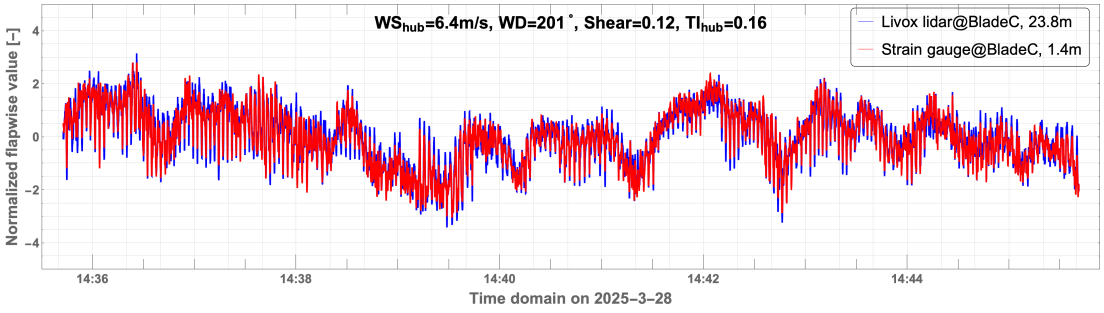

(a)

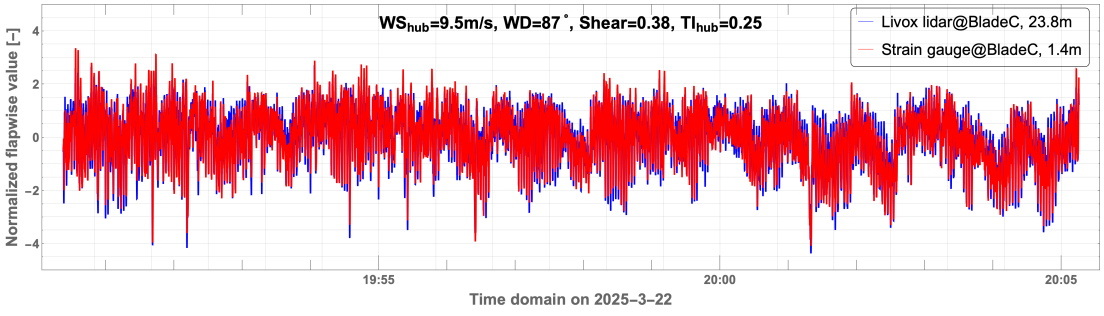

(b)

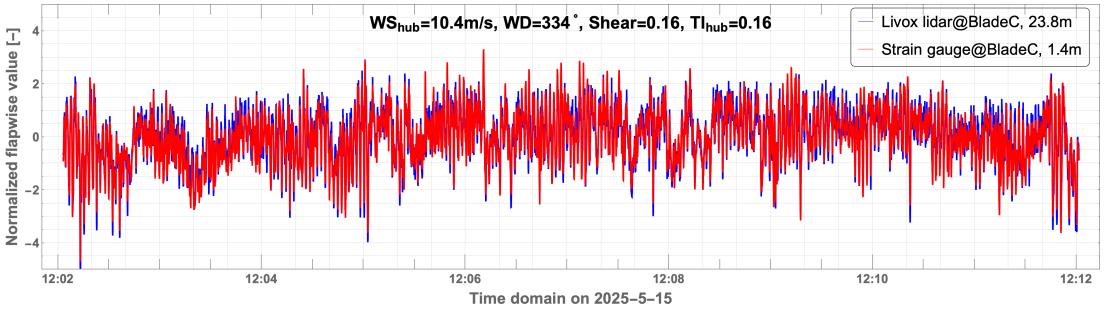

(c)

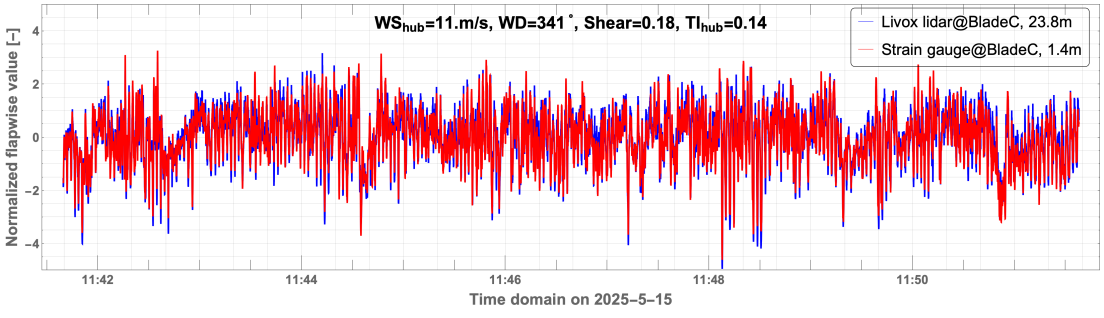

(d)

Figure A1. Normalized flapwise deflection validation: Livox lidar vs. strain gauge bending moments under different wind conditions.

https://doi.org/10.5194/wes-2026-104
Preprint. Discussion started: 3 July 2026

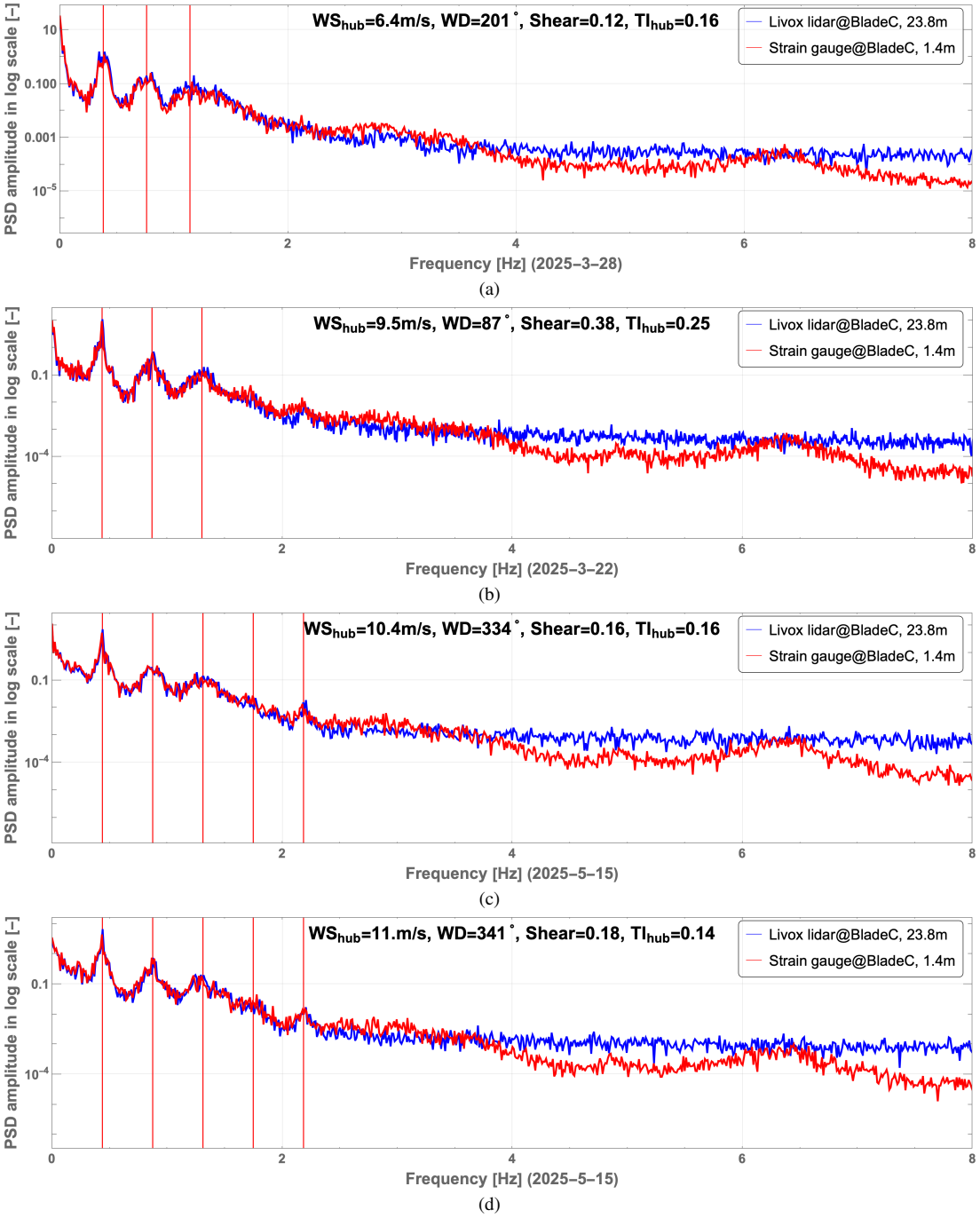

Figure A2. Spectral validation of normalized flapwise deflection: Livox lidar vs. strain gauge data under different wind conditions.

https://doi.org/10.5194/wes-2026-104
Preprint. Discussion started: 3 July 2026

eawe european academy of wind energy
Open Access WIND ENERGY SCIENCE DISCUSSIONS

Appendix B: Comparative Analysis of Blade Pitch Angle

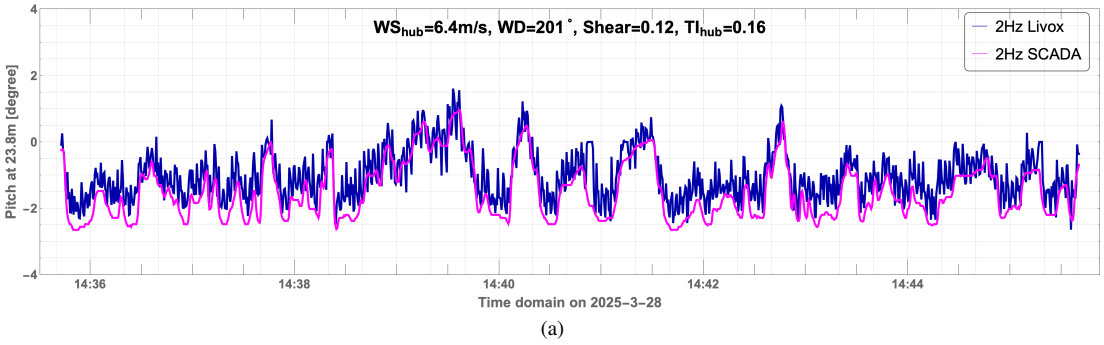

(a)

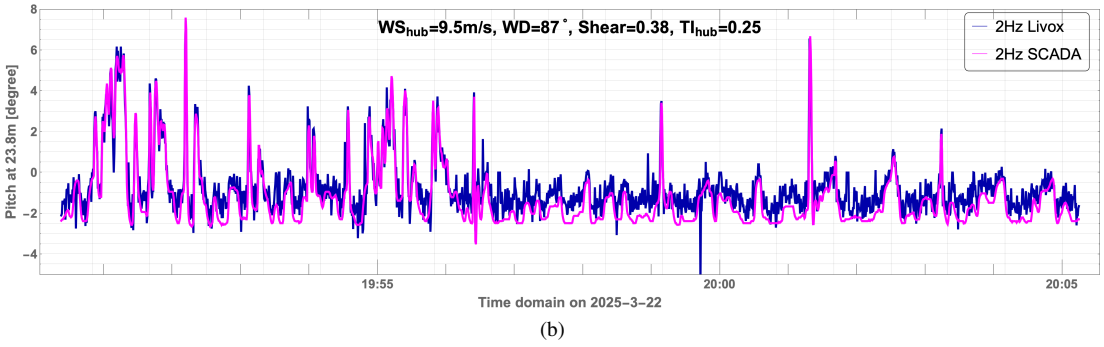

(b)

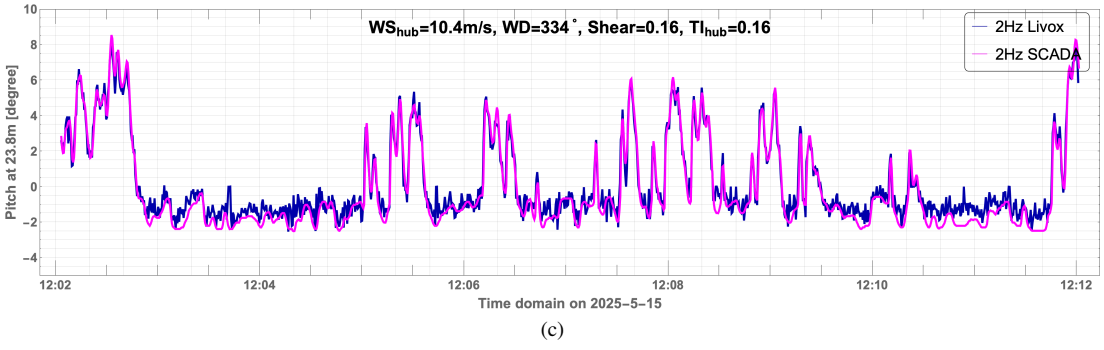

(c)

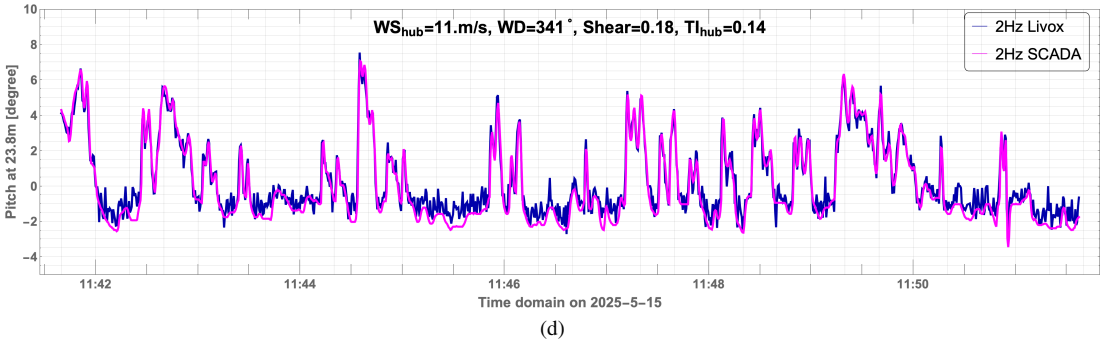

(d)

Figure B1. Comparison of 2 Hz blade pitch angle from Livox lidar measurements and SCADA data across various wind conditions.

https://doi.org/10.5194/wes-2026-104
Preprint. Discussion started: 3 July 2026

eawe european academy of wind energy
Open Access WIND ENERGY SCIENCE DISCUSSIONS

References

Abari, C. F., Pedersen, A. T., and Mann, J.: An all-fiber image-reject homodyne coherent Doppler wind lidar, Optics express, 22, 25 880–25 894, 2014.

Abir, T. A., Kuantama, E., Han, R., Dawes, J., Mildren, R., and Nguyen, P.: Towards robust lidar-based 3D detection and tracking of uavs, in: Proceedings of the Ninth Workshop on Micro Aerial Vehicle Networks, Systems, and Applications, pp. 1–7, 2023.

Amador, S. D., Rasmussen, S., Brincker, R., Rex, S., Skog, M., and Gjødvad, J. F.: Vibration-based FE-model updating for strain history estimation of a 3MW offshore wind turbine tower, in: Journal of Physics: Conference Series, vol. 2647, p. 182035, IOP Publishing, 2024.

Arsenault, T. J., Achuthan, A., Marzocca, P., Grappasonni, C., and Coppotelli, G.: Development of a FBG based distributed strain sensor system for wind turbine structural health monitoring, Smart Materials and Structures, 22, 075 027, 2013.

Behera, A. and Gambier, A.: Multi-objective optimal tuning of the multi-loop pitch control systems of a wind turbine, in: 2018 Annual American Control Conference (ACC), pp. 3068–3073, IEEE, 2018.

Bistline, J. E., Hodson, E., Rossmann, C. G., Creason, J., Murray, B., and Barron, A. R.: Electric sector policy, technological change, and US emissions reductions goals: Results from the EMF 32 model intercomparison project, Energy Economics, 73, 307–325, 2018.

Bouckaert, S., Pales, A. F., McGlade, C., Remme, U., Wanner, B., Varro, L., D'Ambrosio, D., and Spencer, T.: Net zero by 2050: A roadmap for the global energy sector, International Energy Agency, 2021.

Carr, J., Baqersad, J., Niezrecki, C., and Avitabile, P.: Full-field dynamic strain on wind turbine blade using digital image correlation techniques and limited sets of measured data from photogrammetric targets, Experimental Techniques, 40, 819–831, 2016.

Civera, M. and Surace, C.: Non-destructive techniques for the condition and structural health monitoring of wind turbines: A literature review of the last 20 years, Sensors, 22, 1627, 2022.

Fallais, D., Weijtjens, W., and Devriendt, C.: Resolving the effects of peak-splitting alike artefacts in FBG measurements for fatigue assessments of an offshore wind turbine foundation, in: Journal of Physics: Conference Series, vol. 2647, p. 182032, IOP Publishing, 2024.

Fantidis, J., Potolias, C., and Bandekas, D.: Wind turbine blade nondestructive testing with a transportable radiography system, Science and Technology of Nuclear Installations, 2011, 347 320, 2011.

Fung, Y. C.: An introduction to the theory of aeroelasticity, Courier Dover Publications, 2008.

Grundkötter, E. and Melbert, J.: Precision blade deflection measurement system using wireless inertial sensor nodes, Wind Energy, 25, 432–449, 2022.

Hellstein, P. and Szwedo, M.: 3D thermography in non-destructive testing of composite structures, measurement science and technology, 27, 124 006, 2016.

Hung, Y.: Applications of digital shearography for testing of composite structures, Composites Part B: Engineering, 30, 765–773, 1999.

IEA, I.: Net zero roadmap: a global pathway to keep the 1.5° C goal in reach, International Energy Agency Report, 2023.

Jin, L. and Mann, J.: Automotive lidars for monitoring rotating wind turbine blades, in: 2026 The Science of making Torque from wind, p. 062055, IOP Publishing, 2026.

Jin, L., Mann, J., and Sjöholm, M.: Investigating suppression of cloud return with a novel optical configuration of a doppler lidar, Remote Sensing, 14, 3576, 2022.

Jin, L., Mann, J., Angelou, N., and Sjöholm, M.: Suppression of precipitation bias in wind velocities from continuous-wave Doppler lidars, Atmospheric Measurement Techniques, 16, 6007–6023, 2023.

https://doi.org/10.5194/wes-2026-104
Preprint. Discussion started: 3 July 2026

Khadka, A., Dong, Y., and Baqersad, J.: Structural health monitoring of wind turbines using a digital image correlation system on a UAV, in: Rotating Machinery, Optical Methods & Scanning LDV Methods, Volume 6: Proceedings of the 37th IMAC, A Conference and Exposition on Structural Dynamics 2019, pp. 85–91, Springer, 2019.

Kverno, J., Iliev, I., Solemslie, B. W., and Dahlhaug, O. G.: Calibration of strain gauges on a model runner blade combining numerical and experimental data, in: Journal of Physics: Conference Series, vol. 2629, p. 012009, IOP Publishing, 2023.

Lally, E. M., Reaves, M., Horrell, E., Klute, S., and Froggatt, M. E.: Fiber optic shape sensing for monitoring of flexible structures, in: Sensors and Smart Structures Technologies for Civil, Mechanical, and Aerospace Systems 2012, vol. 8345, pp. 831–839, SPIE, 2012.

Lazard, N.: Lazard's Levelized Cost of Energy Analysis—Version 13.0, Lazard Zurich, Switzerland, 2019.

Lee, K., Aihara, A., Puntsagdash, G., Kawaguchi, T., Sakamoto, H., and Okuma, M.: Feasibility study on a strain based deflection monitoring system for wind turbine blades, Mechanical Systems and Signal Processing, 82, 117–129, 2017.

Lehnhoff, S., Gómez González, A., and Seume, J. R.: Full-scale deformation measurements of a wind turbine rotor in comparison with aeroelastic simulations, Wind Energy Science, 5, 1411–1423, https://doi.org/10.5194/wes-5-1411-2020, 2020.

Leica Geosystems: Introduction of Leica Total Station, https://leica-geosystems.com/products/total-stations, last access: 10 June 2026.

Livox Tech: Avia LiDAR Sensor, https://www.livoxtech.com/avia, last accessed: 10 June 2026, 2025.

Mäder, T., Navarro y de Sosa, I., Senf, B., Wolf, P., Hamm, M., Zoch, M., and Drossel, W. G.: Highly elastic strain gauges based on shape memory alloys for monitoring of fibre reinforced plastics, Key Engineering Materials, 742, 778–785, 2017.

Marks, R., Gillam, C., Clarke, A., Armstrong, J., and Pullin, R.: Damage detection in a composite wind turbine blade using 3D scanning laser vibrometry, Proceedings of the Institution of Mechanical Engineers, Part C: Journal of Mechanical Engineering Science, 231, 3024–3041, 2017.

Mishnaevsky Jr, L.: Repair of wind turbine blades: Review of methods and related computational mechanics problems, Renewable energy, 140, 828–839, 2019.

Nelder, J. A.: Downhill simplex method, Computer journal, 7, 308–313, 1965.

Noyes, C., Qin, C., Loth, E., and Schreck, S.: Measurements and predictions of wind turbine tower shadow and fairing effects, Journal of Wind Engineering and Industrial Aerodynamics, 179, 297–307, 2018.

Pietzcker, R. C., Ueckerdt, F., Carrara, S., De Boer, H. S., Després, J., Fujimori, S., Johnson, N., Kitous, A., Scholz, Y., Sullivan, P., et al.: System integration of wind and solar power in integrated assessment models: a cross-model evaluation of new approaches, Energy Economics, 64, 583–599, 2017.

Poozesh, P., Baqersad, J., Niezrecki, C., and Avitabile, P.: A multi-camera stereo DIC system for extracting operating mode shapes of large scale structures, in: Advancement of Optical Methods in Experimental Mechanics, Volume 3: Proceedings of the 2015 Annual Conference on Experimental and Applied Mechanics, pp. 225–238, Springer, 2016.

Poozesh, P., Baqersad, J., Niezrecki, C., Avitabile, P., Harvey, E., and Yarala, R.: Large-area photogrammetry based testing of wind turbine blades, Mechanical Systems and Signal Processing, 86, 98–115, https://doi.org/10.1016/j.ymssp.2016.09.021, 2017.

Qiao, W. and Lu, D.: A survey on wind turbine condition monitoring and fault diagnosis—Part I: Components and subsystems, IEEE transactions on industrial electronics, 62, 6536–6545, 2015a.

Qiao, W. and Lu, D.: A survey on wind turbine condition monitoring and fault diagnosis—Part II: Signals and signal processing methods, IEEE Transactions on Industrial Electronics, 62, 6546–6557, 2015b.

Rizk, P., Al Saleh, N., Younes, R., Ilinca, A., and Khoder, J.: Hyperspectral imaging applied for the detection of wind turbine blade damage and icing, Remote Sensing Applications: Society and Environment, 18, 100 291, 2020.

https://doi.org/10.5194/wes-2026-104
Preprint. Discussion started: 3 July 2026

Schroeder, K., Ecke, W., Apitz, J., Lembke, E., and Lenschow, G.: A fibre Bragg grating sensor system monitors operational load in a wind turbine rotor blade, Measurement science and technology, 17, 1167–1172, 2006.

Wang, P., Zhou, W., Bao, Y., and Li, H.: Ice monitoring of a full-scale wind turbine blade using ultrasonic guided waves under varying temperature conditions, Structural control and health monitoring, 25, e2138, 2018.

Wu, R., Zhang, D., Yu, Q., Jiang, Y., and Arola, D.: Health monitoring of wind turbine blades in operation using three-dimensional digital image correlation, Mechanical Systems and Signal Processing, 130, 470–483, 2019.

Yankova, G. G. and Kock, C. W.: Measurement System and Calibration report, no. 1224 (EN) in DTU Wind Energy WTT I, DTU Wind Energy, Denmark, this is an internal report and therefore not available in full text. Please contact author's or director of author's department for further information., 2018.

Zahle, F., Barlas, A., Lønbæk, K., Bortolotti, P., Zalkind, D., Wang, L., Labuschagne, C., Sethuraman, L., and Barter, G.: Definition of the IEA wind 22-megawatt offshore reference wind turbine, 2024.

Zhong, S.: Progress in terahertz nondestructive testing: A review, Frontiers of Mechanical Engineering, 14, 273–281, 2019.